

Comparisons and quality control of wind observations in a mountainous city using wind profile radar and the Aeolus satellite

**Hua Lu^{1,3}, Min Xie^{1,2}, Wei Zhao⁴, Bojun Liu⁵, Tijian Wang¹,
Bingliang Zhuang¹**

¹School of Atmospheric Sciences, Nanjing University, Nanjing 210023, China

²School of Environment, Nanjing Normal University, Nanjing 210023, China

³Chongqing Institute of Meteorological Sciences, Chongqing 401147, China

⁴Nanjing Institute of Environmental Sciences, Ministry of Ecology and Environment of the
People's Republic of China, Nanjing 210023, China

⁵Chongqing Meteorological Observatory, Chongqing 401147, China

1 Comparisons and quality control of wind observations 2 in a mountainous city using wind profile radar and the 3 Aeolus satellite

4 Hua Lu^{1,3}, Min Xie^{1,2}, Wei Zhao⁴, Bojun Liu⁵, Tijian Wang¹, Bingliang Zhuang¹

5 ¹School of Atmospheric Sciences, Nanjing University, Nanjing 210023, China

6 ²School of Environment, Nanjing Normal University, Nanjing 210023, China

7 ³Chongqing Institute of Meteorological Sciences, Chongqing 401147, China

8 ⁴Nanjing Institute of Environmental Sciences, Ministry of Ecology and Environment of the People's
9 Republic of China, Nanjing 210023, China

10 ⁵Chongqing Meteorological Observatory, Chongqing 401147, China

11 *Correspondence to:* Min Xie (minxie@nju.edu.cn) , Wei Zhao (zhaowei@nies.org)

12 **Abstract:** Observations of vertical wind profile in Chongqing, a typical mountainous city in China,
13 are important, but sparse and have low resolution. To obtain more wind profile data, this study
14 matched the Aeolus track with ground-based wind observation sites in Chongqing in 2021. Based on
15 the obtained results, verification and quality control studies were conducted on the wind observations
16 of a wind profile radar (WPR) with radiosonde (RS) data, and a comparison of the Aeolus Mie-cloudy
17 and Rayleigh-clear wind products with WPR data was then performed. The conclusions can be
18 summarized as follows: (1) A clear correlation between the wind observations of WPR and RS was
19 found, with a correlation coefficient (R) of 69.92%. Their root-mean-square deviation increased with
20 height, but decreased at height between 3 and 4 km. (2) After quality control of Gaussian filtering
21 (GF) and empirical orthogonal function construction (EOFc, G = 87.23%) of the WPR data, the R
22 between the WPR and RS reached 76.00% and 95.44%, respectively. The vertical distribution showed
23 that GF could better retain the characteristics of WPR wind observations, but with limited
24 improvement in decreasing deviations, whereas EOFc performed better in decreasing deviations, but
25 considerably modified the original characteristics of the wind field, especially regarding intensive
26 vertical wind shear in strong convective weather processes. (3) In terms of the differences between
27 the Aeolus and WPR data, 56.0% and 67.8% deviations were observed within ± 5 m/s for
28 Rayleigh-clear and Mie-cloudy winds vs. WPR winds, respectively. Vertically, large mean
29 differences of both Rayleigh-clear and Mie-cloudy winds versus WPR winds appeared below 1.5 km,
30 which is attributed to the prevailing quiet and small winds within the boundary layer in Chongqing, in
31 this case the movement of molecules and aerosols is mostly affected by irregular turbulence.

32 Additionally, large mean differences at the height range between 4 to 8 km for Mie-cloudy versus
33 WPR winds may be related to the high content of cloud liquid water in the middle troposphere of
34 Chongqing. (4) The differences in both Rayleigh-clear and Mie-cloudy versus WPR winds had
35 changed. Deviations of 58.9% and 59.6% were concentrated between ± 5 m/s for Rayleigh-clear
36 versus WPR winds with GF and EOFc quality control, respectively. In contrast, 69.1% and 70.2% of
37 deviations appeared between ± 5 m/s for Rayleigh-clear versus WPR and EOFc WPR winds,
38 respectively. These results shed light on the comprehensive applications of multi-source wind profile
39 data in mountainous cities or areas with sparse ground-based wind observations.

40 **Keywords:** Wind profile radar, Aeolus satellite, data verification, data quality control, mountainous
41 city

42 **1 Introduction**

43 The detection of the atmospheric wind profile is essential for studying atmospheric dynamics,
44 interactions between weather and pollution, and predict extreme weather (Baker et al., 1995; King et
45 al., 2017; Stettner et al., 2019; Sun et al., 2022). Furthermore, the value of atmospheric wind
46 observations has been illustrated by assimilation applications in numerical weather prediction
47 (Benjamin et al., 2004; Weissmann and Cardinali, 2007; Michelson and Bao, 2008). In particular,
48 wind fields within the boundary layer are mostly turbulent and difficult to simulate using models
49 without the assimilation of wind observations (Belmonte and Stoffelen 2019; Simonin et al., 2014).
50 For areas with complex terrain, such as mountainous cities, individual ground-based observation
51 stations usually have poor representation, and thus vertical observations are essential (Sekula et al.,
52 2021; Lu et al., 2022b). Therefore, unconventional wind profile observations are urgently required for
53 analysis and assimilation into numerical prediction models to describe the transport of mesoscale
54 weather systems, as well as to advance our knowledge of atmospheric component movement in the
55 actual atmosphere.

56 Wind profile radar (WPR) data may partially compensate for the limitations of conventional
57 wind field observations. WPR detects the scattering effect of atmospheric turbulence on
58 electromagnetic waves to detect the Doppler effect signals of air movement, and is capable of
59 providing horizontal wind vectors with high temporal and vertical resolution (Weber et al., 1990;
60 Dibbern et al., 2001). The automated, continuous, and real-time vertical wind profiles from the WPR

61 could fill the gaps in upper-air observations, both in time continuity and vertical resolution. Terrain
62 and climate characteristics in unique regions could have different impacts on WPR echoes, resulting
63 in separate data observation errors. Therefore, data verification, and occasionally adequate quality
64 control, are required before the application of WPR data in a specific region (Zhang et al., 2015; Guo
65 et al., 2020). In comparison, radiosonde (RS) data are often considered reliable atmospheric wind
66 observations to verify WPR data (Weber et al., 1990; Chen et al., 2021).

67 Owing to advances in satellite detection, wind fields acquired from satellites can supplement
68 conventional ground-based observations in space coverage. Atmospheric motion vector detection can
69 only extract the wind information of layers with clouds. The United States and Europe have
70 successively detected sea surface wind fields using microwave radiometers and scatterometers
71 (Endlich et al., 1971; Njoku et al., 1980; Gaiser et al., 2004; Barre et al., 2008). The World
72 Meteorological Organization regards the detection of global three-dimensional wind fields as one of
73 the most challenging and important meteorological observation missions in the 21st century (WMO,
74 2001). The United States and Europe have conducted space-borne wind lidar measurement programs,
75 as these are the best methods for detecting three-dimensional wind fields (Beranek et al., 1989; Baker
76 et al., 2008; Wernham et al., 2016). The Aeolus satellite was launched following the European Space
77 Agency's (ESA) fifth Earth Explorer mission on August 22, 2018. As the world's first Doppler wind
78 lidar in space, Aeolus has enabled the continuous detection of global wind profiles from the ground to
79 the lower stratosphere with a vertical resolution of 0.25–1 km (Marseille et al., 2008; Reitebuch et al.,
80 2006; Zhang et al., 2019). Therefore, the wind profile data detected by Aeolus can compensate for the
81 lack of spatial coverage and vertical resolution of ground-based wind field observations to some
82 extent.

83 Located at the edge of the Sichuan Basin, Chongqing is a typical mountainous city in China
84 known for its complex topography. Owing to the unique terrain, the mechanism of extreme weather
85 and movement of atmospheric components in the city are intricate and complex, making vertical
86 observations essential. Interference sources for the vertical detection of WPR might form in
87 mountainous areas, which are different from those in plain areas. Thus, reasonable data verification
88 and quality control should be conducted before application to ensure the accuracy and
89 representativeness of the WPR. The spatial distribution of ground-based vertical wind observations in
90 Chongqing is sparse, and it is worthwhile to verify the performance of Aeolus wind products and

91 apply them to related mechanistic studies or numerical assimilation systems. To this end, wind profile
92 observations of RS, WPR, and Aeolus were collected and matched in terms of time and space for
93 2021 in Chongqing. Based on the matched results, data verification and quality control of WPR wind
94 observations were implemented using RS data, and the performance of Aeolus wind products in
95 Chongqing was analyzed to provide a scientific basis for multi-source wind profile data applications
96 in mountainous cities. The remainder of this paper is organized as follows: the RS, WPR, and Aeolus
97 data used in this study, the matching procedure, data verification, and quality control methods are
98 described in Section 2; Section 3 presents the comparison and quality control results of the WPR and
99 Aeolus wind profile data; finally, the main conclusions are summarized in Section 4.

100 **2 Data and methods**

101 **2.1 Data**

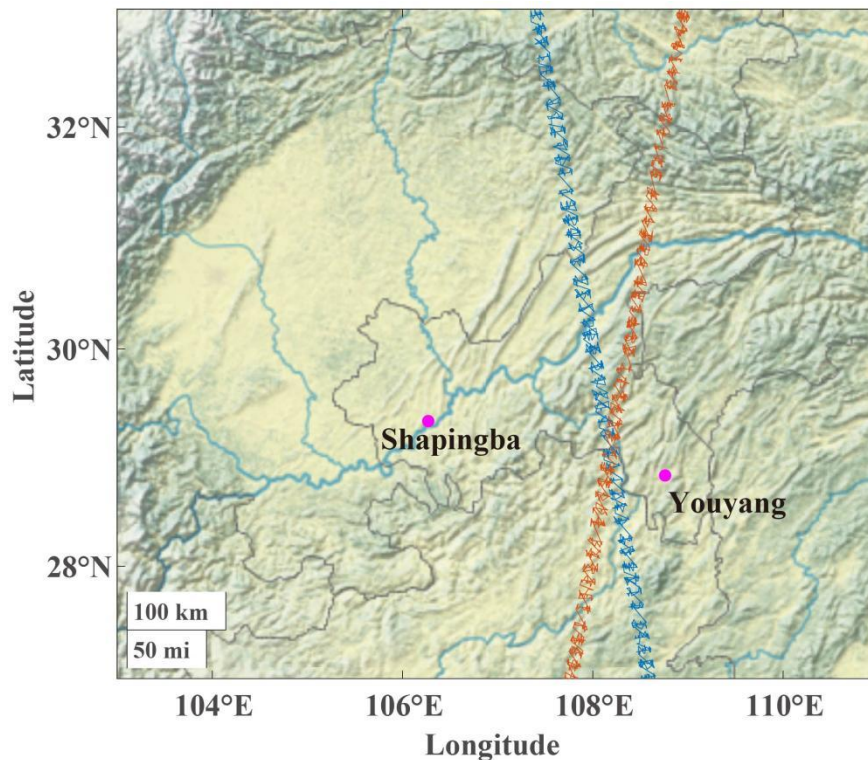
102 **2.1.1 Ground-based wind profile data**

103 Shapingba (57516; 106.27°E, 29.34°N) is a national weather station and the only RS station in
104 Chongqing. Wind speed and direction at 0000 and 1200 UTC (universal time coordinated) were
105 obtained from an L-band sounding system on vertical height levels every 1 s from the surface to 30
106 km in the air (Zhang et al., 2020). Shapingba station belonged to the network of the L-band sounding
107 system by China Meteorological Administration. The operational radiosonde stations in China widely
108 use GTS1 digital radiosonde as key components of L-band sounding system, which have high
109 accuracy within the troposphere in detecting fine resolution profiles of meteorological factors (Bian et
110 al., 2011; Guo et al., 2016; Guo et al., 2021b).

111 There are two wind profile radars in Chongqing, one at Shapingba station and the other at
112 Youyang station (57633; 108.76 ° E, 28.84 ° N). Radars can operate almost automatically and
113 continuously, acquiring vertical profiles of horizontal wind speed and wind direction (Guo et al.,
114 2021a). The WPR in Shapingba and Youyang are from the same manufacturer, sharing the same
115 temporal and spatial vertical resolutions of 5 min and 120 m, and vertically detecting 48 and 45 layers
116 up to 9360 and 8910 m, respectively.

117 RS wind data are generally reliable vertical observations. Considering Shapingba WPR is
118 located at the same station with RS, while Youyang Station is 360 km away from the RS, therefore,

119 the data verification of WPR wind observations was conducted based on Shapingba WPR and RS
120 data in this study (Figure 1).



121
122 **Figure 1. Geographic locations of ground-based wind observation stations and Aeolus tracks along within**
123 **Chongqing. The magenta dots denote ground-based observation stations, while red and blue line represent**
124 **Aeolus tracks. The background is the terrain heights.**

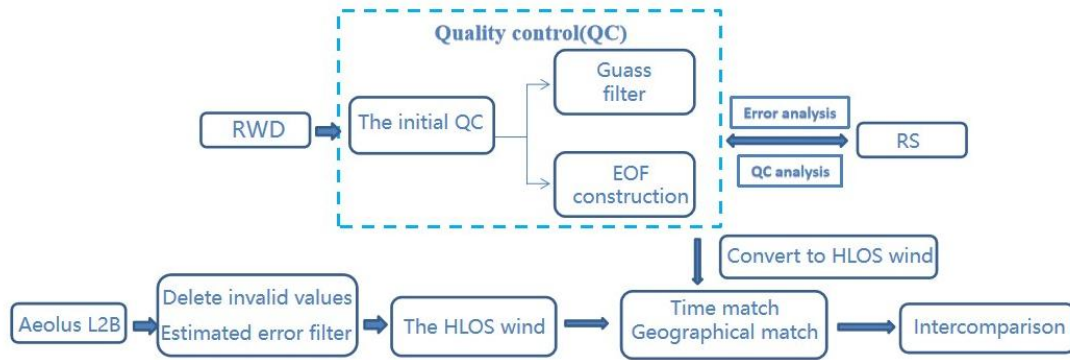
125 **2.1.2 Aeolus wind products**

126 Launched on August 22, 2018, the first space-borne Doppler wind lidar, Aeolus, developed by
127 the ESA, has been circling in a sun-synchronous orbit at an altitude of approximately 320 km, with a
128 7-day repeat cycle (ESA, 2008). Based on the original detection information, a series of products was
129 released by the ESA. The Aeolus Level-2B products can provide scientific wind products, which can
130 be used to obtain wind profile data from the ground to approximately 30 km in the air, with a vertical
131 resolution of 0.25–2 km and an uncertainty of 2–4 m/s, varying with height (Rennie, 2018; Chen et al.,
132 2022). Level-2B wind products are classified into Rayleigh-clear and Mie-cloudy winds. Specifically,
133 Rayleigh channels mainly detect wind fields with atmospheric molecules as tracers in the troposphere
134 and lower stratosphere, whereas the Mie channel detects signals from aerosols and cloud droplet
135 particles within the boundary layer or in the cloud (Witschas et al., 2020). In this study, the horizontal
136 line-of-sight (HLOS) wind products of both Rayleigh and Mie channels were used. Additionally, the

137 validity flag and estimated errors were extracted for quality control of HLOS wind products (Tan et
138 al., 2017; Guo et al., 2021a).

139 2.2 Methods

140 2.2.1 Data matching and verification procedures



141 **Figure 2: Flowchart of the multi-source wind profile data matching and verification procedures.**

142 In an attempt to make full use of the multi-source vertical wind data from Chongqing,
143 appropriate procedures were used to match the RS, WPR, and Aeolus data in time and space
144 considering the limited ground-based wind profile observations. A flowchart of the procedure is
145 shown in Figure 2.

146 First, data verification and quality control effect analysis of the Shapingba WPR were
147 implemented based on RS data. Based on the approach used by Zhang et al. (2016) and Guo et al.
148 (2021a), the Aeolus data were removed once the distances between adjacent tracks of Aeolus and
149 ground-based sites exceeded 1° . With this procedure, Shapingba station is not suitable for comparison
150 with Aeolus data, whereas Youyang WPR data is. Time and space matches of the WPR and Aeolus
151 data were posed before the comparison, the geographic location of WPR stations and Aeolus tracks
152 are shown in Figure 1. Specifically, because of the higher temporal resolution of WPR, the mean
153 values of WPR data within 10 min before and after Aeolus sampling were used. Vertically, Aeolus
154 data were interpolated and matched to the layers of WPR data. Subsequently, Aeolus data were
155 screened by validity flags and estimated errors. Thereafter, both the original Youyang WPR detection
156 and quality control data were converted into HLOS winds for comparison with the Aeolus data. The
157 WPR wind vector was projected onto the HLOS winds using the following equation (Witschas et al.,
158 2020):

159
$$v_{RWP_{HLOS}} = \cos(\psi_{Aeolus} - wd_{RWP}) \cdot ws_{RWP} \quad (1)$$

160 where ψ_{Aeolus} is the Aeolus azimuth angle, which could be extracted from the Level 2B products,
 161 while wd_{RWP} and ws_{RWP} are WPR wind direction and speed, respectively.

162 **2.2.2 Statistical method**

163 The mean bias (MB) and root mean squared error (RMSE) were adopted as indicators (Equations
 164 2 and 3) for the verification of the WPR and Aeolus wind products, which compares absolute and
 165 relative deviations, respectively.

166
$$MB = \frac{1}{n} \sum_{i=1}^n (o(i) - r(i)) \quad (2)$$

167
$$RMSE = \sqrt{\frac{\sum_{i=1}^n (o(i) - r(i))^2}{n}} \quad (3)$$

168 where $o(i)$ represents the observation values and $r(i)$ represents the referent values.

169 **2.2.3 Data quality control of the wind profile radar**

170 **2.2.3.1 The initial quality control**

171 The first step in quality control is to eliminate the abnormal increase of horizontal wind in a
 172 small vertical range of WPR data, including screening invalid data exceeding the climate extreme
 173 values and the vertical consistency test. The extreme climate wind values on the relative layers (Zuo
 174 2020) are listed in Table 1. For the vertical consistency test, if the wind difference between a specific
 175 layer and its adjacent layer is greater than three times that of the two layers below, the value is
 176 considered as an abnormal observation to be deleted (Zhang et al., 2015).

177 **Table 1: Extreme climate wind values in vertical layers**

Pressure(hPa)	1000	850	700	500	400	300	250
Height(m)	0	1500	3000	5500	7000	9000	10000
Extreme wind(m/s)	36.01	46.30	61.73	102.89	128.61	154.33	154.33

178 **2.2.3.2 Gaussian filtering (GF) method**

179 GF is a smooth filtering method that can be used to smooth out the details and noise of
 180 two-dimensional graphs, and the observed value of the central point and its surrounding values are
 181 summed in one-to-one correspondences. GF is similar to mean filtering, but its preset convolution
 182 operator presents a Gaussian distribution. In this study, the convolutional operator was used to
 183 calculate the weighted average of the WPR data to filter the high-frequency noise in the observation

184 of WPR. The Gaussian filtering function of the one-dimensional zero-mean normalization is as
 185 follows:

$$186 \quad g(x) = \frac{1}{\sqrt{2\pi}\sigma} e^{-\frac{x^2}{2\sigma^2}} \quad (4)$$

187 where σ is the scale factor that determines the width of the Gaussian filter and further affects the
 188 degree of data smoothing. The larger the σ value, the wider the frequency band of the Gaussian filter,
 189 and the better the data smoothing effect. However, an excessively large σ value causes excessive
 190 data loss and distortion. In this study, σ was set to 3.

191 2.2.3.3 Empirical orthogonal function construction (EOFc) method

192 Based on the spatial-temporal sequence formed by wind field data W , calculations similar to
 193 empirical orthogonal decomposition were performed, and the main modes obtained by calculation
 194 were used to reconstruct the spatial-temporal sequence to construct new wind fields. Specifically, the
 195 X matrix is formed by selecting N times, a period of time before and after a certain moment, and L
 196 layers of effective data, vertically. X is represented below:

$$197 \quad X = \begin{bmatrix} W_{1,1} & W_{1,2} & \cdots & W_{1,N} \\ W_{2,1} & W_{2,2} & \cdots & W_{2,N} \\ \vdots & \vdots & \ddots & \vdots \\ W_{L,1} & W_{L,2} & \cdots & W_{L,N} \end{bmatrix} \quad (5)$$

198 Subsequently, the covariance matrix of X , that is, $S = XX^T$, and its eigenvalues and eigenvectors
 199 were calculated. According to the arrangement of the eigenvalues from largest to smallest, the
 200 cumulative interpretation variance of the first m eigenvectors can be expressed as follows:

$$201 \quad G = \left(\sum_{k=1}^m \lambda_k \right) / \left(\sum_{k=1}^L \lambda_k \right) \quad (6)$$

202 The larger the eigenvalue corresponding to the eigenvector, the more its corresponding
 203 distribution reflects the typical characteristics of the original field. The time coefficient $T = ETX$ was
 204 calculated with the eigenvector E . Finally, the main modes decomposed by EOF were used to
 205 reconstruct the time series within N times, following the use of $X = ET$ to obtain the vertical
 206 distribution of the wind field at the corresponding time. In the reconstruction of the time series, a
 207 cut-off threshold ($G \geq 85\%$) was set for the interpretation of the cumulative variance to control the
 208 quality of the observed data.

209 Assuming that the cumulative interpretation variances of the first m feature vectors met $G \geq 85\%$,
210 and the first $m-1$ did not meet $G \geq 85\%$, the feature vectors of the first m modes were adopted in the
211 reconstruction of the sequence, and the corresponding winds at moment j of the i th altitude layer are:

$$212 \quad WS_{i,j} = \sum_{k=1}^m e_{i,k} t_{k,j} \quad (7)$$

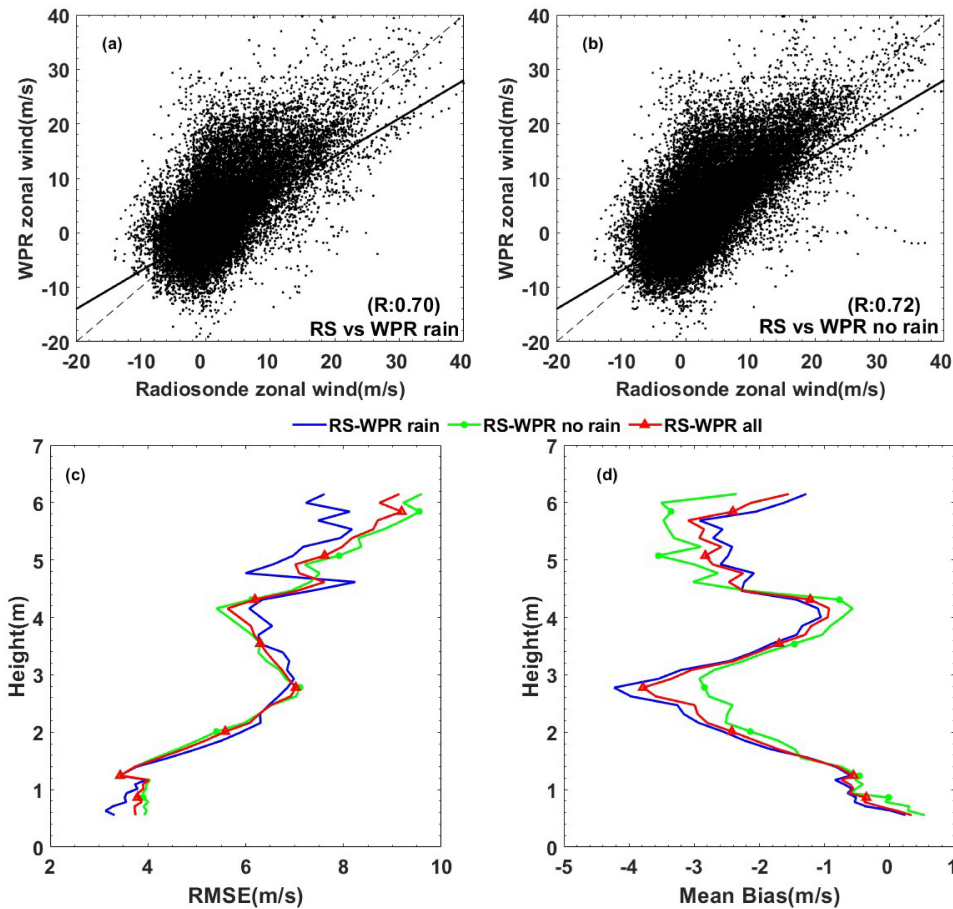
213 The EOFc method can eliminate outliers and pulsating noise from observation data, and has been
214 applied in quality control research of observational elements in previous studies, such as in Qin et al.
215 (2010).

216 **2.2.4 Quality control of Aeolus wind products**

217 The quality of the Aeolus HLOS wind products is controlled by validity flags and estimated
218 errors, which are also present in Level 2 B data products. Only data with flags equal to 1 were
219 considered valid. The data were subsequently filtered according to estimated errors, the theoretical
220 values calculated based on the measured signal levels, and the temperature and pressure sensitivity of
221 the Rayleigh channel response (Dabas et al., 2008). Previous studies have revealed that notable
222 observation errors appeared when the estimated errors were large (Witschas et al., 2020).
223 Consequently, thresholds for estimated errors of 7(5) m/s were applied for Rayleigh(Mie) winds in
224 this study, based on the method described by Guo et al. (2021a).

225 **3 Results and discussion**

226 **3.1 Data verification and quality control of WPR**



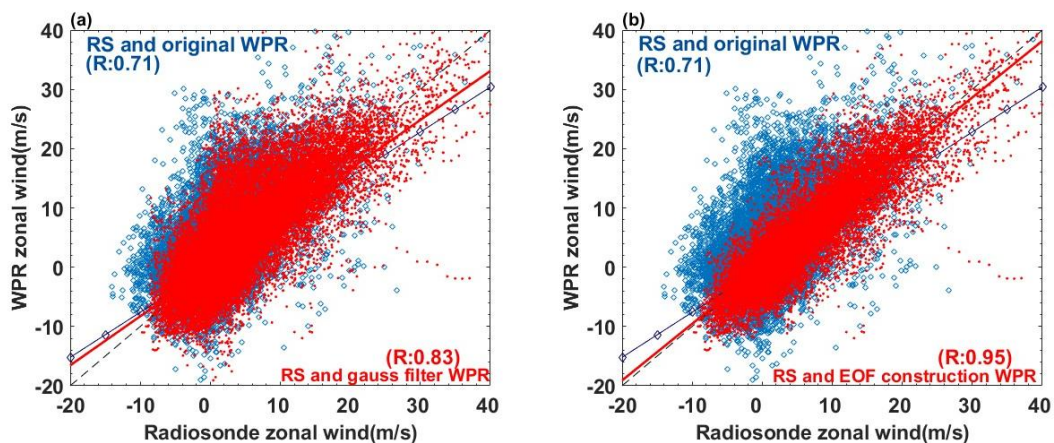
227

228 **Figure 3. Scatter-plots for wind profile radar (WPR) vs radiosonde (RS) data during (a) rainy days and (b)**
229 **no rainy days, and vertical distribution of (c) root mean squared error (RMSE) and (d) mean bias (MB)**
230 **for WPR vs RS during all days, rainy days and no rainy days.**

231 Data verification and quality control of the Shapingba WPR were performed based on RS data
232 from the same station. The WPR detects data vertically above the station, while the RS data are
233 derived from air balls, which can respectively drift as far as 0-90, 2-25 and <10km at 200, 500 and
234 850hPa away from the releasing station (Zeng et al., 2019). Therefore, certain differences exist in the
235 spatial sampling of WPR and RS. Assuming that the atmospheric horizontal distribution is uniform
236 within dozens of kilometers, the WPR and RS wind fields will be comparable. Additionally, the exact
237 release times of the air balls were 23:15 and 11:15 UTC, and they generally take 25 min to rise to 10
238 km. Therefore, the mean values of the 23:15–00:00 and 11:15–12:00 WPR data were processed to
239 compare the WPR and RS data. Finally, for comparison with the Aeolus data, wind fields derived

240 from WPR and RS data were converted into zonal wind components for data verification and quality
241 control.

242 To clarify influences of weather, especially precipitation, on wind profile radar observation
243 quality, scatter plots and vertical distribution of statistical parameters for WPR versus RS during rainy
244 days and no rainy days were given in Figure 3. Between 1.5 and 4.5 km, WPR deviations during rainy
245 days exceeded a little that without rain, and the RMSE and MB between WPR and RS were slightly
246 smaller during rainy days than that without rain below 1.5km and above 4.5km. The correlation
247 coefficient between WPR and RS with rain was a bit lower than that without rain. Generally speaking,
248 precipitation could affect WPR observation quality, but the deviation distributions were overall the
249 same during rainy and no rainy days, with slight differences on different layers. As a result, we
250 discussed the quality control effects of WPR data based on all data, including rainy days and no rain
251 days.



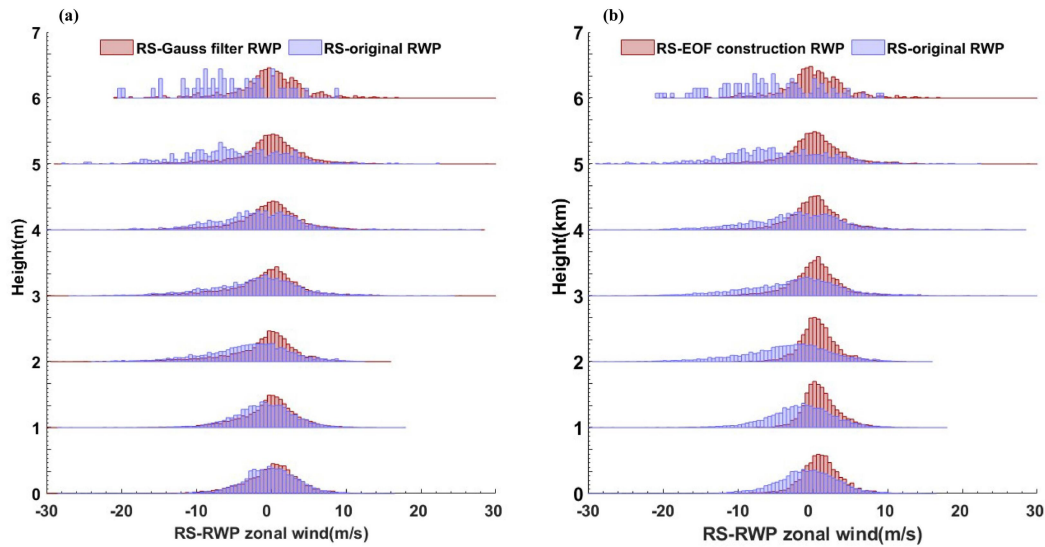
252

Figure 4: Scatter-plots for (a) original and Gaussian filtering (GF) WPR vs RS data, (b) original and empirical orthogonal function construction (EOFc) WPR vs RS data.

253

254 Based on quality control 1 of the WPR data mentioned above, 784 invalid wind speed data were
255 filtered, after which GF and EOFc were conducted on WPR winds. The blue dots in Figure 4
256 represent the scattered distributions of the original WPR and RS data. The correlation coefficient(R)
257 was 69.92%, with scatters distributed along the reference line, indicating a correlation between the
258 two types of data. Large numbers of dots with significant deviations from the reference line between
259 the wind speeds of ± 10 m/s implied large differences between the WPR and RS in the observation
260 of low wind speeds. The red dots in Figure 4(a) are scatter plots of GF-controlled WPR and RS, with
261 an R of 76.00%, showing better correlation compared with the original WPR and RS wind data. The

262 GF method screened parts of the data far away from the reference line, which are wind data with large
 263 differences between WPR and RS, contributing to an improvement in the correlation of the two types
 264 of data. The performance of the WPR data quality control based on EOFc is more significant in
 265 Figure 4(b) compared to GF. For EOFc, G was selected to be greater than 85% for the first time;
 266 specifically, the first two modes were added after EOF decomposition, with $G = 87.23\%$. The R
 267 between the EOFc WPR and RS winds reached 95.44%, with scatters more concentrated around the
 268 reference line compared with the original and GF WPR.



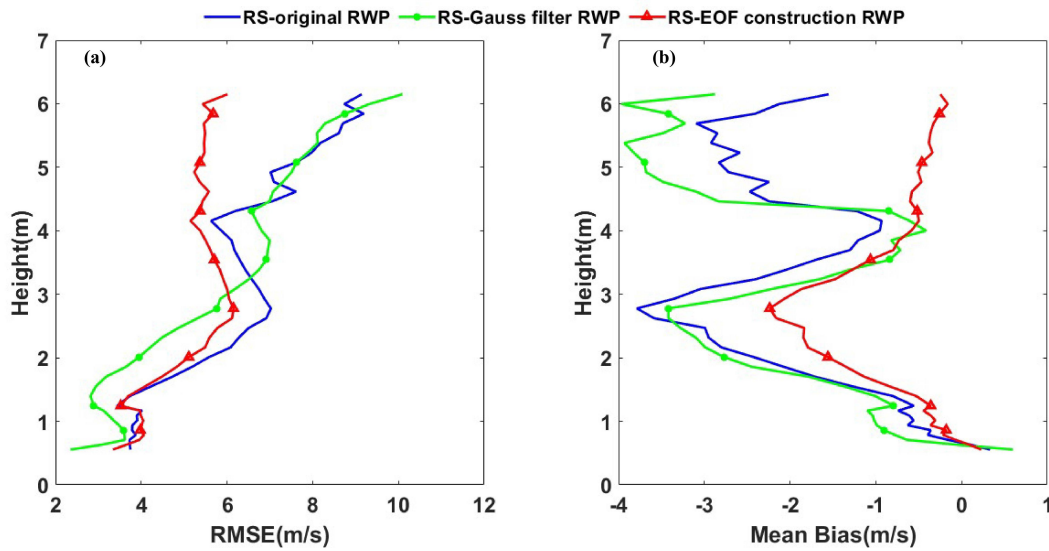
269

Figure 5: Probability density distributions vertical variations of (a) RS minus original and GF WPR data, (b) RS minus EOFc WPR data.

270

271 The vertical wind deviation distributions of the original and quality-controlled WPR are shown
 272 in Figure 5, and the vertical distributions of the statistical parameters are shown in Figure 5. The
 273 distribution of deviations between the RS and original WPR data followed normal distribution on
 274 various layers. The median of the distribution was centred around 0 near ground within 2km, and
 275 gradually moved towards to the negative values above 2km, indicating significant negative deviations
 276 on the upper layers. Large negative deviations emerged on different layers, however, large positive
 277 deviations were mainly distributed around 3-5 km, with the maximum around 30 m/s. From the
 278 perspective of statistical parameters, the RMSE of RS and the original WPR deviation increased with
 279 height overall, but decreased at heights between 3 and 4 km. The vertical MB distribution between the
 280 RS and original WPR data presented an M-shaped distribution, with positive MB values near the
 281 ground and negative values in the other layers. According to the vertical distribution of the deviation

282 scatter points, the negative deviations are significantly larger than the positive deviations. For a
 283 relatively small MB value of approximately 4 km, some of the large positive deviations in Figure 5 at
 284 this level balance the negative values. Similarly, large positive and negative deviations appeared at
 285 approximately 6 km, forming small MB values at this level. In general, wind speeds increase with
 286 height, leading to an increase in the observation deviations of the WPR.



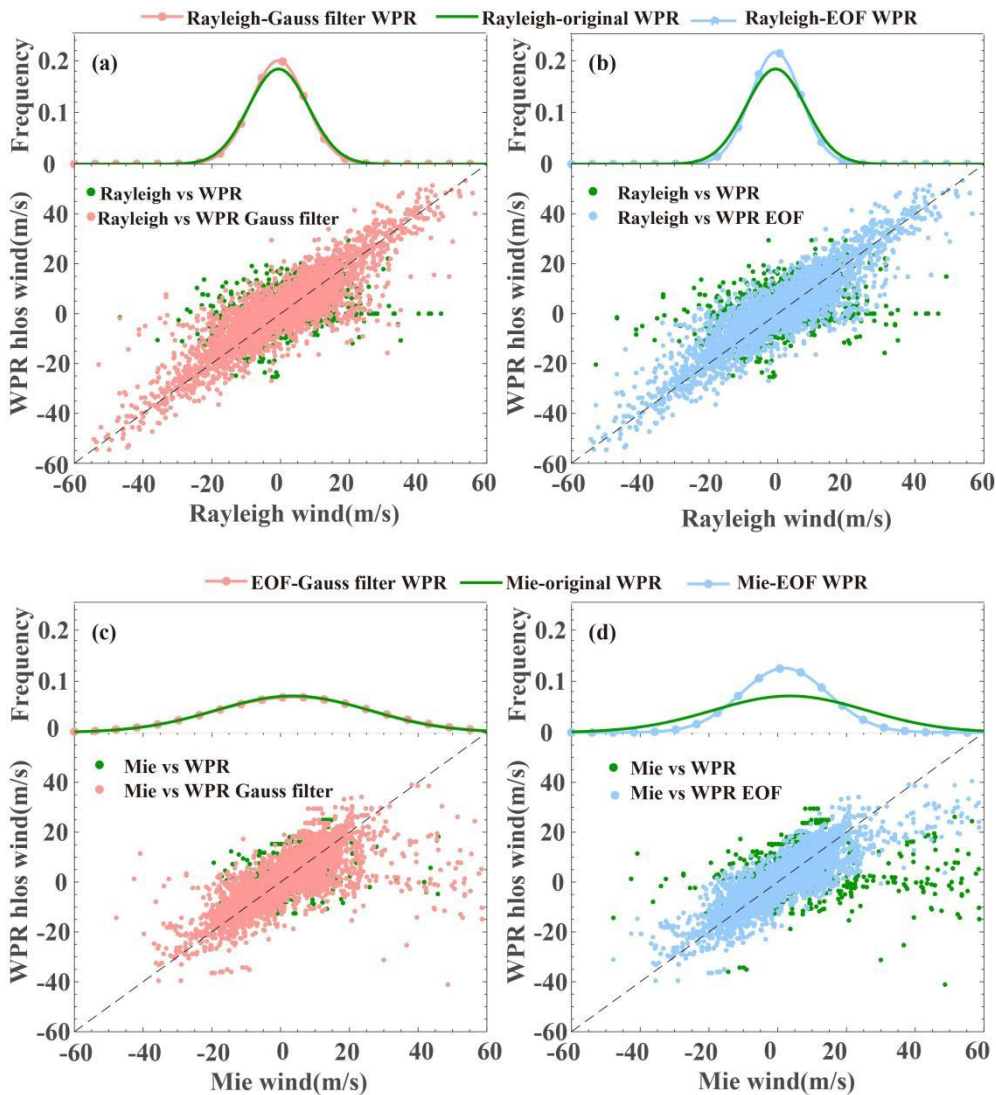
287

Figure 6: Vertical distributions of RMSE and MB for (a) RS vs GF WPR data, (b) RS vs EOFc WPR data.

288

289 Taking RS data as true values, the zonal WPR wind data in Chongqing exhibited various
 290 detection errors with height, indicating that quality control of the original WPR data is necessary. The
 291 red histograms in Figure 5(a) represent the vertical deviation distributions between RS data and the
 292 GF WPR with respect to height. Compared with the original WPR data, GF eliminates some large
 293 deviation values of different layers, making the distribution more centred around 0, especially on the
 294 upper layers. The vertical distributions of the RMSE and MB between the RS and WPR data
 295 corresponded to modifications. The RMSE of the RS and GF WPR data is reduced below 3 km
 296 compared to the original WPR, while the alteration of MB mainly manifests above 4 km. Remarkably,
 297 the negative value of MB above 4 km increased after GF in the WPR data. This was because of the
 298 reduction in the larger positive deviation value, and the negative deviation could not be offset.
 299 Subsequently, the EOFc method was adopted for the zonal winds in the original WPR data. The
 300 vertical deviation distributions of RS and EOFc WPR reduced many large negative deviations in the
 301 different vertical layers, making distribution more in line with normal distribution(Figure 5b). The

302 statistical parameters of the vertical distribution also showed significant changes compared to the
303 original data. A significant decrease in the RMSE value and a notable reduction in the negative MB
304 above 1 km were observed between the RS and EOFc WPR (Figure 6). Combining both the vertical
305 distribution for deviation scatters and statistical parameters, the EOFc WPR winds were similar to the
306 RS data at various heights. Although the deviations of the two types of data were significantly
307 reduced, it is worth noting that the EOFc WPR data have modified the characteristics of the original
308 wind fields to a large extent, especially under strong convective weather conditions with large vertical
309 wind shear. In comparison, the GF WPR data could better retain the basic characteristics of the
310 original wind fields. However, the GF method exhibited a limited reduction in the detection
311 deviations of the WPR data. In general, the two quality control methods have different effects on the
312 reduction of detection deviations and the retention of the original information.



314

Figure 7: Probability density distributions of deviations and scatter-plots between (a) Rayleigh-clear and (c) Mie-cloudy vs WPR original and GF WPR winds, (b) Rayleigh-clear and (d) Mie-cloudy vs original and EOFc WPR winds.

315

316

317

318

319

320

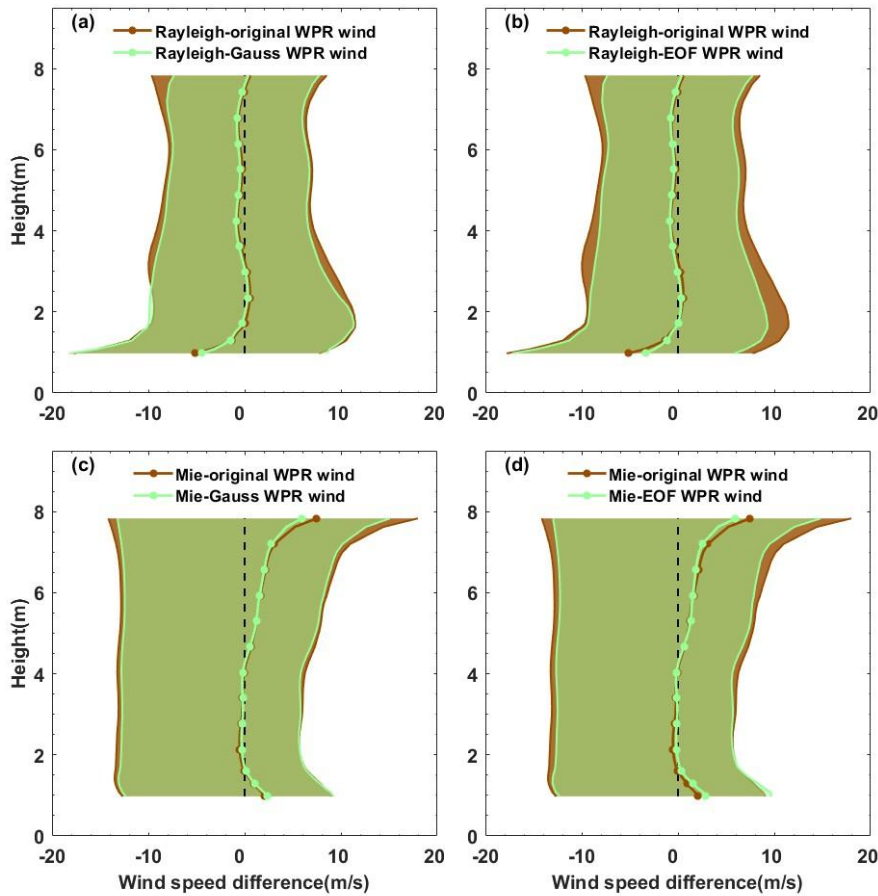
321

322

323

Owing to the limited spatial coverage of ground-based wind profile data, data verification of Aeolus products in Chongqing was conducted to compensate for the spatial coverage of wind observations to some extent. The obtained results indicate that the Youyang WPR data can be used to verify the Aeolus products described in Section 2. The probability density distribution (PDD) and scatter plots of both Aeolus Rayleigh-clear and Mie-cloudy products versus WPR data are shown in Figure 7. The PDD of deviations between Rayleigh-clear and WPR in Figure 7(a) generally present as a Gaussian distribution, with 82.9% of deviations concentrated between ± 10 m/s and 56.0% of deviations between ± 5 m/s. Quality control with the GF and EOFc methods was conducted on

324 original WPR observations, and the PDD of deviations between Rayleigh-clear and quality-controlled
325 WPR winds were concentrated around 0. For deviations between Rayleigh-clear and GF WPR winds,
326 85.8% of deviations were centralized between ± 10 m/s and 58.9% of deviations between ± 5 m/s.
327 In comparison, 86.3% of deviations of Rayleigh-clear and EOFc WPR winds appeared between ± 10
328 m/s and 59.6% of deviations between ± 5 m/s. The scatter distributions of the Rayleigh-clear and
329 WPR winds were shown in Figure 7(a) and 7(b), respectively. A good correlation between
330 Rayleigh-clear and original WPR data was observed, except for some dots far from the reference line,
331 which were scattered with large deviations between the Aeolus and WPR data. Better correlations
332 were observed between the Rayleigh-clear and quality-controlled WPR winds with more scatter
333 centralized around the reference line. Figure 7(c)–(d) show the PDD distribution and scatter plots of
334 the deviations between the Mie-cloudy and WPR winds. 86.2% of deviations of Mie-cloudy versus
335 original WPR data were centralized between ± 10 m/s and 67.8% of deviations between ± 5 m/s,
336 while 86.9% of deviations of Mie-cloudy versus GF WPR winds were centralized between ± 10 m/s
337 and 69.1% of deviations between ± 5 m/s. For the EOFc WPR winds, 87.5% of deviations appeared
338 between ± 10 m/s and 70.2% of deviations between ± 5 m/s. First, the deviations of the Mie-cloudy
339 and quality-controlled WPR data were more concentrated around 0 compared with the original RWP.
340 Most of the scatter points between the Mie-cloudy and original RWP winds were centralized near the
341 reference line. However, a number of dots were concentrated around ± 20 m/s for the WPR winds,
342 and much larger values for the Aeolus data appeared away from the reference line. Additionally,
343 compared with Rayleigh-clear winds, deviations in the Mie-cloudy versus WPR data were small,
344 which may be attributed to the detection principles of the two channels. Compared with the Rayleigh
345 channel, the tracers for the Mie channel, including aerosols and cloud droplets within the boundary
346 layer and in the cloud, mainly centralized at lower vertical levels with smaller wind speeds, resulting
347 in smaller wind deviations for the Mie-cloudy observations.



348

Figure 8: Vertical distribution of mean differences and deviations between (a) Rayleigh-clear vs GF WPR data, (b) Rayleigh-clear vs original and EOFc WPR data, (c) Mie-cloudy vs original and GF WPR data and (d) Mie-cloudy vs original and EOFc WPR data.

349

350 Figure 8 shows the vertical distribution characteristics of the differences between Aeolus
 351 products and RWP data. The red solid line represents the vertical distributions of the mean differences
 352 between Aeolus and the original RWP data, and the shaded areas denote positive and negative
 353 deviations from the mean differences. Mean differences between the Rayleigh-clear and original
 354 WPR winds have large negative deviations below 1.5 km, with the maximum deviation reaching
 355 -5.2-13.0, -5.2+12.61 m/s. However, the mean difference between these data maintained within ± 1
 356 m/s from the heights of 1.5 to 8km, with simultaneous decreasing negative and positive deviations
 357 with height. The wind measurement capability of the Rayleigh channel is largely limited by the
 358 receiving intensity, and the Sichuan Basin is one of the large-value aerosol regions in China (Zhang et
 359 al., 2012; Lu et al., 2022a). Particularly, below 1.5 km within the boundary layer, strong aerosol

360 scattering will inevitably affect molecular scattered signals, thus reducing the accuracy of Rayleigh
361 channel wind field inversion (Tan et al., 2017; Guo et al., 2021a). In contrast, the vertical distribution
362 of mean differences between Mie-cloudy and original RWP data (Figure 8c and d) showed large
363 values within the boundary layer (below 1.5 km) and middle troposphere (4–8 km). The maximal
364 deviation within the boundary layer reached 2.09-18.23, 2.09+14.76 m/s, while the maximal values
365 were 7.49-19.98, 7.49+21.64 m/s in the middle troposphere. For the Mie channel, aerosols and cloud
366 droplet particles were used as tracers for wind measurements. Owing to the influence of the
367 topography in Chongqing, the prevailing quiet and small winds within the boundary layer result in the
368 dominant influence of turbulent motion on large particles (Lu et al., 2022b). This contributes to larger
369 deviations in Mie wind observations because of the irregularity of turbulence. The notable mean
370 differences in the middle troposphere may be affected by the distribution of cloud droplets. Previous
371 studies have revealed that due to the influence of the topography of the Tibetan Plateau, the liquid
372 cloud water contents around 27°N to 35°N in central China are remarkably larger than those in the
373 southern and northern regions at the same altitude (Yang et al., 2012), with nimbostratus and
374 altostratus prevailing in the affected areas (Yu et al., 2004). These may contribute to large mean
375 differences and deviations between Mie winds and WPR data at altitudes of 4–8 km in Chongqing,
376 which is located on the eastern side of the Tibetan Plateau. According to existing observations, the
377 frequency of cloud occurrence in the middle troposphere in spring, autumn, and winter is higher than
378 that in summer, which can explain to some extent why the annual mean differences between Mie
379 winds and RWP around 4–8 km have large values, whereas the average values in summer do not
380 (Guo et al., 2021a). Based on the GF and EOFc quality control of the WPR data, the mean differences
381 between the Rayleigh-clear and WPR winds were found to not change significantly, with only some
382 reduction in the differences between the Rayleigh-clear and EOFc WPR data within the boundary
383 layer. However, by controlling the WPR data quality, the positive and negative deviations of the mean
384 difference at various heights can be effectively reduced (Figure 8a and 6b). Specifically, GF can
385 reduce deviations above 3 km, whereas EOFc modifies the positive deviations within the boundary
386 layer. For the Mie winds, a remarkable reduction was observed for mean differences at an altitude of
387 approximately 6–8 km and deviations in various layers with quality-controlled WPR data compared
388 with the original WPR data.

389 4 Conclusions

390 To evaluate the observation quality of the multi-source wind profile data in Chongqing, this
391 study matched the Aeolus, RS, and WPR data for 2021. The matching results indicate that the
392 Youyang WPR can be used for comparison with the Aeolus winds. Additionally, data verification and
393 quality control studies of ground-based WPR data were conducted based on Shapingba RS wind
394 observations. The main conclusions are as follows:

395 A correlation was found between the RS and original WPR zonal wind data, with an R of
396 69.92% and scatter points generally distributed along the reference line. The RMSEs of the RS and
397 WPR data increased with height overall, except at an increase of approximately 3–4 km. The MB was
398 vertically distributed in an M-shape, with relatively smaller MB values appearing at 4 and 6 km
399 because of the cancellation of positive and negative deviations.

400 Following screened by the extreme wind climate values and the vertical consistency test, 784
401 WPR wind observations were eliminated. The R between RS versus GF WPR data and EOFc (G =
402 87.23) WPR data were 76.00% and 95.44%, respectively, demonstrating a better correlation between
403 RS and EOFc WPR data. A comparison of the deviations in the vertical distribution of the RS and
404 WPR data before and after quality control revealed that the EOFc WPR data are closer to RS winds at
405 various heights, resulting in smaller deviations between the two. However, it should be noted that the
406 EOFc WPR winds have a broader filter than the original data, which can remarkably alter the
407 characteristics of the original wind fields, particularly in cases of severe convection weather
408 conditions where there are significant vertical wind shears. While preserving the basic features of the
409 original wind field, the GF method has a limited impact on reducing the deviations of the original
410 WPR wind observations.

411 The Rayleigh and Mie winds detected by Aeolus exhibited various deviations from the WPR
412 data; 56.0% of deviations between Rayleigh-clear and WPR data existed within ± 5 m/s, while
413 67.8% of deviations exist between Mie-cloudy and 67.8% of deviations between WPR data were
414 within ± 5 m/s. The Mie channel detects aerosols and cloud droplets as tracers, which are lower than
415 the height layers detected by the Rayleigh channel, resulting in relatively small wind speed deviations.
416 However, the mean differences between Rayleigh-clear and WPR winds are smaller than those of
417 Mie-cloudy winds, especially in the middle troposphere of 4–8 km. This may be due to the influence

418 of the topography of the Tibetan Plateau, resulting in a remarkable increase in the liquid cloud water
419 content from 27°N to 35°N in central China compared to other regions. Chongqing is located in the
420 affected areas; thus, the accuracy of Mie wind observations is influenced by the middle troposphere.

421 The deviations between the Aeolus and WPR data changed to some extent after quality control
422 of the WPR data, both for the Rayleigh-clear and Mie-cloudy winds. The scatter points of the Aeolus
423 and WPR data, which were far away from the reference line, decreased; 58.9% of deviations between
424 the Rayleigh-clear and GF WPR data were centralized between ± 5 m/s, and 59.6% of deviations for
425 EOFc WPR data were within ± 5 m/s. For the Mie channel, 69.1% of deviations were concentrated
426 ± 5 m/s between the satellite and GF WPR data, and 70.2% of deviations existed between the Mie
427 and EOFc WPR data. The mean differences of the Rayleigh channel and WPR data changed little
428 after quality control was conducted using both the GF and EOFc methods on WPR data; however,
429 both positive and negative deviations to the mean values decreased. For Mie winds, quality control on
430 WPR made distinct modifications to the mean differences between 6–8 km and deviations to the
431 mean values of all layers between Mie-cloudy and WPR data.

432 **Financial support:** This work was supported by the National Natural Science Foundation of China
433 (42205186), the Chongqing Natural Science Foundation (cstc2021jcyj-msxmX1007), the open
434 research fund of Chongqing Meteorological Bureau (KFJJ-201607), Sichuan Science and Technology
435 Program (2023YFS0430) and the key technology research and development of Chongqing
436 Meteorological Bureau (YWJSGG-202215; YWJSGG-202303).

437 **Acknowledgments:** We would like to express our gratitude to China Meteorological Bureau to provide
438 the ground-based wind profile data, and the European Space Agency to provide the Aeolus wind
439 products.

440 **Conflicts of Interest:** The authors declare no conflict of interest.

441 **Reference**

- 442 Baker W. 2008. Doppler wind lidar: current activities and future plans//Winter T-PARC Workshop.
443 [s.l.]: NOAA/NASA/DoD Joint Center for Satellite Data Assimilation.
- 444 Baker, W. E., Emmitt, G. D., Robertson, F. R., Atlas, R., Molinari, J. E., Bowdle, D. A., Paegle, J. N.,
445 Hardesty, R. M., Menzies, R. T., Krishnamurti, T. N., Brown, R. A., Post, M. J., Anderson, J.
446 R., Lorenc, A. C., and McElroy, J. L. 1995. Lidar-measured winds from space: A key
447 component for weather and climate prediction, *Bulletin of the American Meteorological*
448 *Society* 76, 869-888.

- 449 Barre H M J P, Duesmann B and Kerr Y H. 2008. SMOS: the mission and the system. IEEE
450 Transactions on Geoscience and Remote Sensing, 46(3): 587-593.
- 451 Belmonte Rivas, M., and Stoffelen, A. 2019. Characterizing ERA-Interim and ERA5 surface wind
452 biases using ASCAT, Ocean Sci. 15, 831-852.
- 453 Benjamin, S. G., Schwartz, B. E., Szoke, E. J., and Koch, S. E. 2004. The Value of Wind Profiler
454 Data in U.S. Weather Forecasting, Bulletin of the American Meteorological Society 85,
455 1871-1886.
- 456 Beranek R G, Bilbro J W, Fitzjarrald D E, Jones W D, Keller V W and Perrine B S. 1989. Laser
457 atmospheric wind sounder (LAWS)//Proceedings of SPIE 1062, Laser Applications in
458 Meteorology and Earth and Atmospheric Remote Sensing. Los Angeles: SPIE: 234-248.
- 459 Bian, J., Chen, H., Vömel, H. et al. Intercomparison of humidity and temperature sensors: GTS1,
460 Vaisala RS80, and CFH. Adv. Atmos. Sci. 28, 139–146. 2011.
461 <https://doi.org/10.1007/s00376-010-9170-8>
- 462 Chen, C., Xue, X., Sun, D., Zhao, R., Han, Y., Chen, T., et al. 2022. Comparison of lower
463 stratosphere wind observations from the USTC's Rayleigh Doppler lidar and the ESA's
464 satellite mission Aeolus. Earth and Space Science, 9, e2021EA002176.
- 465 Chen, Z.-Y., Chu, Y.-H., and Su, C.-L. 2021. Intercomparisons of Tropospheric Wind Velocities
466 Measured by Multi-Frequency Wind Profilers and Rawinsonde, Atmosphere 12, 1284.
- 467 Dabas, A., Denneulin, M. L., Flamant, P., Loth, C., Garnier, A., and Dolfi-Bouteyre, A.: Correcting
468 winds measured with a Rayleigh Doppler lidar from pressure and temperature effects, Tellus
469 A, 60, 206–21.
- 470 Endlich R M, Wolf D E, Hall D J and Brain A E. 1971. Use of a pattern recognition technique for
471 determining cloud motions from sequences of satellite photographs. Journal of Applied
472 Meteorology, 10(1): 105-117.
- 473 European Space Agency (ESA): “ADM-Aeolus Science Report,” 2008. ESA SP-1311, 121 p.,
474 http://esamultimedia.esa.int/docs/SP-1311_ADM-Aeolus_FINAL_low-res.pdf,
- 475 Gaiser P W, St Germain K M, Twarog E M, Poe G A, Purdy W, Richardson D, Grossman W, Jones
476 W L, Spencer D, Golba G, Cleveland J, Choy L, Bevilacqua R M and Chang P S. 2004. The
477 WindSat spaceborne polarimetric microwave radiometer: sensor description and early orbit
478 performance. IEEE Transactions on Geoscience and Remote Sensing, 42(11): 2347-2361.
- 479 Guo, J., Liu, B., Gong, W., Shi, L., Zhang, Y., Ma, Y., Zhang, J., Chen, T., Bai, K., Stoffelen, A., de
480 Leeuw, G., and Xu, X. 2021. Technical note: First comparison of wind observations from
481 ESA's satellite mission Aeolus and ground-based radar wind profiler network of China,
482 Atmos. Chem. Phys. 21, 2945-2958.

483 Guo, J., Miao, Y., Zhang, Y., Liu, H., Li, Z., Zhang, W., He, J., Lou, M., Yan, Y., Bian, L., and Zhai,
484 P. 2016. The climatology of planetary boundary layer height in China derived from
485 radiosonde and reanalysis data, *Atmos. Chem. Phys.*, 16, 13309–13319,
486 <https://doi.org/10.5194/acp-16-13309-2016>.

487 Guo, J., Zhang, J., Yang, K., Liao, H., Zhang, S., Huang, K., Lv, Y., Shao, J., Yu, T., Tong, B., Li, J.,
488 Su, T., Yim, S. H. L., Stoffelen, A., Zhai, P., and Xu, X. 2021. Investigation of near-global
489 daytime boundary layer height using high-resolution radiosondes: first results and
490 comparison with ERA5, MERRA-2, JRA-55, and NCEP-2 reanalyses, *Atmos. Chem. Phys.*,
491 21, 17079–17097, <https://doi.org/10.5194/acp-21-17079-2021>.

492 King, G. P., Portabella, M., Lin, W., and Stoffelen, A. 2017. Correlating extremes in wind and stress
493 divergence with extremes in rain over the Tropical Atlantic, EUMETSAT Ocean and Sea Ice
494 SAF Scientific Report OSI_AV5_15_02, Version 1.0, available at:
495 [http://www.osi-saf.org/?q\\$=_content/correlating-extremeswind-and-stress-divergence-extremes-rain-over-tropical-atlantic](http://www.osi-saf.org/?q$=_content/correlating-extremeswind-and-stress-divergence-extremes-rain-over-tropical-atlantic)).

497 Lu, H., Xie, M., Liu, B., Liu, X., Feng, J., Yang, F., Zhao, X., You, T., Wu, Z., and Gao, Y. 2022a.
498 Impact of atmospheric thermodynamic structures and aerosol radiation feedback on winter
499 regional persistent heavy particulate pollution in the Sichuan-Chongqing region, China,
500 *Science of The Total Environment* 842, 156575.

501 Lu, H., Xie, M., Liu, X., Liu, B., Liu, C., Zhao, X., Du, Q., Wu, Z., Gao, Y., and Xu, L. 2022b.
502 Spatial-temporal characteristics of particulate matters and different formation mechanisms of
503 four typical haze cases in a mountain city, *Atmospheric Environment* 269, 118868.

504 Marseille G J, Stoffelen A and Barkmeijer J. 2008. Impact assessment of prospective spaceborne
505 Doppler wind lidar observation scenarios. *Tellus A: Dynamic Meteorology and*
506 *Oceanography*, 60(2): 234-248.

507 Michelson, S., and Bao, J.-W. 2008. Sensitivity of Low-Level Winds Simulated by the WRF Model
508 in California's Central Valley to Uncertainties in the Large-Scale Forcing and Soil
509 Initialization, *Journal of Applied Meteorology and Climatology - J APPL METEOROL*
510 *CLIMATOL* 47, 3131-3149.

511 Njoku E, Christensen E and Cofield R. 1980. The Seasat scanning multichannel microwave
512 radiometer (SMMR): antenna pattern corrections-Development and implementation. *IEEE*
513 *Journal of Oceanic Engineering*, 5(2): 125-137.

514 Reitebuch O, Paffrath U and Leike I. 2006. ATBD: ADM-Aeolus Level 1B Product. European Space
515 Research and Technology Centre.

516 Rennie, M. P. 2018. An assessment of the expected quality of Aeolus Level-2B wind products, *EPJ*
517 *Web Conf.*, 176, 02015, <https://doi.org/10.1051/epjconf/201817602015>,

- 518 Sekuła, P., Bokwa, A., Bartyzel, J., Bochenek, B., Chmura, Ł., Galkowski, M., and Zimnoch, M.
519 2021. Measurement report: Effect of wind shear on PM10 concentration vertical structure in
520 the urban boundary layer in a complex terrain, *Atmospheric Chemistry & Physics* 21,
521 12113-12139.
- 522 Simonin, D., Ballard, S., and Li, Z. 2014. Doppler radar radial wind assimilation using an hourly
523 cycling 3D-Var with an 1.5km resolution version of the Met Office Unified Model for
524 Nowcasting, *Quarterly Journal of the Royal Meteorological Society* 140.
- 525 Stettner, D., Velden, C., Rabin, R., Wanzong, S., Daniels, J., and Bresky, W. 2019. Development of
526 enhanced vortex-scale atmospheric motion vectors for hurricane applications, *Remote Sens.*,
527 11, 1981, <https://doi.org/10.3390/rs11171981>.
- 528 Sun, X., Zhou, Y., Zhao, T., Bai, Y., Huo, T., Leng, L., He, H., and Sun, J. 2022. Effect of Vertical
529 Wind Shear on PM2.5 Changes over a Receptor Region in Central China, *Remote Sensing*
530 14, 3333.
- 531 Tan, D., Rennie, M., Andersson, E., Poli, P., Dabas, A., de Kloe, J., Marseille, G.-J., and Stoffelen, A.
532 2017. Aeolus Level-2B Algorithm Theoretical Basis Document, Tech. rep.,
533 AE-TN-ECMWFL2BP- 0023, v. 3.0, 109 pp.
- 534 Weber, B. L., & Wuertz, D. B. 1990. Comparison of Rawinsonde and Wind Profiler Radar
535 Measurements, *Journal of Atmospheric and Oceanic Technology*, 7(1), 157-174.
- 536 Weissmann, M., and Cardinali, C. 2007. Impact of airborne Doppler lidar observations on ECMWF
537 forecasts, *Quarterly Journal of the Royal Meteorological Society* 133, 107-116.
- 538 Wernham D, Ciapponi A, Riede W, Allenspacher P, Era F, D'Ottavi A and Thibault
539 D. 2016. Verification for robustness to laser-induced damage for the Aladin instrument on
540 the ADM-Aeolus satellite//Proceedings of SPIE 10014, Laser-Induced Damage in Optical
541 Materials 2016. Boulder: SPIE: 1001408.
- 542 Witschas, B., Lemmerz, C., Geiß, A., Lux, O., Marksteiner, U., Rahm, S., Reitebuch, O., and Weiler,
543 F. 2020. First validation of Aeolus wind observations by airborne Doppler wind lidar
544 measurements, *Atmos. Meas. Tech.* 13, 2381-2396.
- 545 Yang Dasheng, Wang Pucai. 2012. Characteristics of Vertical Distributions of Cloud Water Contents
546 over China during Summer[J]. *Chinese Journal of Atmospheric Sciences*, 36(1): 89-101.
- 547 Yu, R., Wang, B., & Zhou, T. 2004. Climate Effects of the Deep Continental Stratus Clouds
548 Generated by the Tibetan Plateau, *Journal of Climate*, 17(13), 2702-2713.
- 549 Zeng, Z., Mao, F., Wang, Z., Guo, J., Gui, K., An, J., et al . 2019. Preliminary evaluation of the
550 atmospheric infrared sounder water vapor over China against high-resolution radiosonde

- 551 measurements. *Journal of Geophysical Research: Atmospheres*, 124, 3871 – 3888.
552 <https://doi.org/10.1029/2018JD029109>
- 553 Zhang C L, Sun X J, Zhang R W, Zhao S J, Lu W, Liu Y W and Fan Z Q. 2019. Impact of solar
554 background radiation on the accuracy of wind observations of spaceborne Doppler wind
555 lidars based on their orbits and optical parameters. *Optics Express*, 27(12): A936-A952.
- 556 Zhang, W., Guo, J., Miao, Y., Liu, H., Zhang, Y., Li, Z., and Zhai, P. 2016. Planetary boundary layer
557 height from CALIOP compared to radiosonde over China, *Atmos. Chem. Phys.* 16,
558 9951-9963.
- 559 Zhang Xubin, Wan Qilin, Xue Jishan, Ding Weiyu, Li Haorui. 2015. Quality control of wind profile
560 radar data and its application to assimilation[J]. *Acta Meteorologica Sinica*, (1): 159-176.
- 561 Zhang, X., Wang, Y., and Niu, T. 2012. Atmospheric aerosol compositions in China: Spatial/temporal
562 variability, chemical signature, regional haze distribution and comparisons with global
563 aerosols, *Atmos Chem Phys* 58, 26571-26615.
- 564 Zhang, Y., J. Guo, Y. Yang, Y. Wang, and S.H.L. Yim. 2020. Vertical wind shear modulates
565 particulate matter pollutions: A perspective from Radar wind profiler observations in Beijing,
566 China. *Remote Sensing*, 12(3), 546.
- 567 Zuo Q. M.S. 2020. Research on Quality Control Methods and Assimilation Application of Wind
568 Profiler Radar Data. Nanjing: Nanjing University of Information Science and Technology.